Gate-tunable imbalanced Kane-Mele model in encapsulated bilayer jacutingaite

Louk Rademaker [1] and Marco Gibertini [2,3]

[1] *Department of Theoretical Physics, University of Geneva, CH-1211 Geneva, Switzerland*

[2] *Dipartimento di Scienze Fisiche, Informatiche e Matematiche, University of Modena and Reggio Emilia, I-41125 Modena, Italy*

[3] *Department of Quantum Matter Physics, University of Geneva, CH-1211 Geneva, Switzerland*

(Received 21 July 2020; revised 24 February 2021; accepted 24 March 2021; published 9 April 2021)

We study free, capped, and encapsulated bilayer jacutingaite (Pt_2HgSe_3) from first principles. While the freestanding bilayer is a large-gap trivial insulator, we find that the encapsulated structure has a small trivial gap due to the competition between sublattice symmetry breaking and sublattice-dependent next-nearest-neighbor hopping. Upon the application of a small perpendicular electric field, the encapsulated bilayer undergoes a topological transition towards a quantum spin Hall insulator. We find that this topological transition can be qualitatively understood by modeling the two layers as uncoupled and can be described by an imbalanced Kane-Mele model that takes into account the sublattice imbalance and the corresponding inversion-symmetry breaking in each layer. Within this picture, bilayer jacutingaite undergoes a transition from a 0+0 state, where each layer is trivial, to a 0+1 state, where an unusual topological state relying on Rashba-like spin orbit coupling emerges in only one of the layers.

DOI: 10.1103/PhysRevMaterials.5.044201

I. INTRODUCTION

Topological insulators have a finite gap in their bulk energy spectrum but differ from standard (trivial) insulators because a nonzero topological invariant is associated with the manifold of occupied states [1,2]. In most cases, the nontrivial topological invariant results in the appearance of metallic states that cross the bulk gap close to the boundary of a finite-size system. The nature of the topological invariant depends on the dimensionality and the underlying fundamental symmetries of the system [3,4], including crystal symmetries [5,6]. A paradigmatic example is the integer quantum Hall state in two dimensions (2D), for which the topological invariant is an integer C, known as the Chern number, which provides the number of (chiral) states localized close to each edge and is related to the quantized Hall conductivity $\sigma_{xy} = C\, e^2/h$ [7,8].

When time-reversal symmetry is preserved in 2D, although the Chern number vanishes identically, another topological invariant ν can be introduced [9–12], which is a $\mathbb{Z}_2$ number that can assume only two values: 0 or 1, i.e., trivial or nontrivial. As a consequence of time-reversal symmetry, gapless states appear at the edges of the system in pairs of counterpropagating (helical) modes, and a bulk-boundary correspondence relates ν to the parity of the number of such pairs. In particular, we have that an even number of helical pairs is topologically trivial ($\nu = 0$), as states belonging to different pairs can be mixed and adiabatically gapped out without breaking time-reversal symmetry. On the contrary, time-reversal-invariant topological insulators ($\nu = 1$), also known as quantum spin Hall insulators (QSHIs), have an odd number of pairs, so that the presence at each edge of at least one pair of helical gapless states is robust.

Experimental realizations of the QSHI phase have been reported in semiconductor quantum wells based on HgTe/CdTe [13–16] and InAs/GaSb [17,18] heterostructures, as well as in two-dimensional materials like WTe_2 [19–22]. In all these systems, the operating conditions where transport is dominated by edge states are limited to fairly low temperatures owing to their small bulk energy gap. A breakthrough could be represented by monolayer Pt_2HgSe_3, which has been predicted using first-principles simulations to be the first materials realization of the seminal Kane-Mele model [9,10] for QSHIs, with a substantial energy gap of 0.5 eV [23] (and could even give rise to a Chern insulator when functionalized [24] or interfaced with a magnetic material like CrI_3 [25]). Although monolayers of this material could be potentially exfoliated [26] from a bulk layered mineral called jacutingaite [27,28], a clear experimental validation is still lacking [29].

When two QSHI monolayers are stacked together to form a bilayer, the system is expected to become trivial in the limit of weak interlayer coupling. Indeed, when the layers are almost independent, we inevitably have an overall even number of helical pairs that can hybridize and get gapped out, consistent with the fact that the bulk topological invariant is defined only modulo 2, so that $\nu_{\text{bi}} = \nu_{\text{mono}} + \nu_{\text{mono}} = 1 + 1 \equiv 0 \mod 2$. Analogously, a trilayer should be nontrivial, and for thicker layers we would expect an alternation of trivial and nontrivial topologies that, in the bulk limit, would give rise to a weak topological phase [30] relying on the translational invariance along the stacking direction.

In bulk jacutingaite, the layers cannot be considered nearly as independent, so that this scenario is expected to break down. Indeed, first-principles simulations have shown that nearby layers are strongly hybridized, giving rise to a large second-nearest-layer hopping [31]. This strong coupling

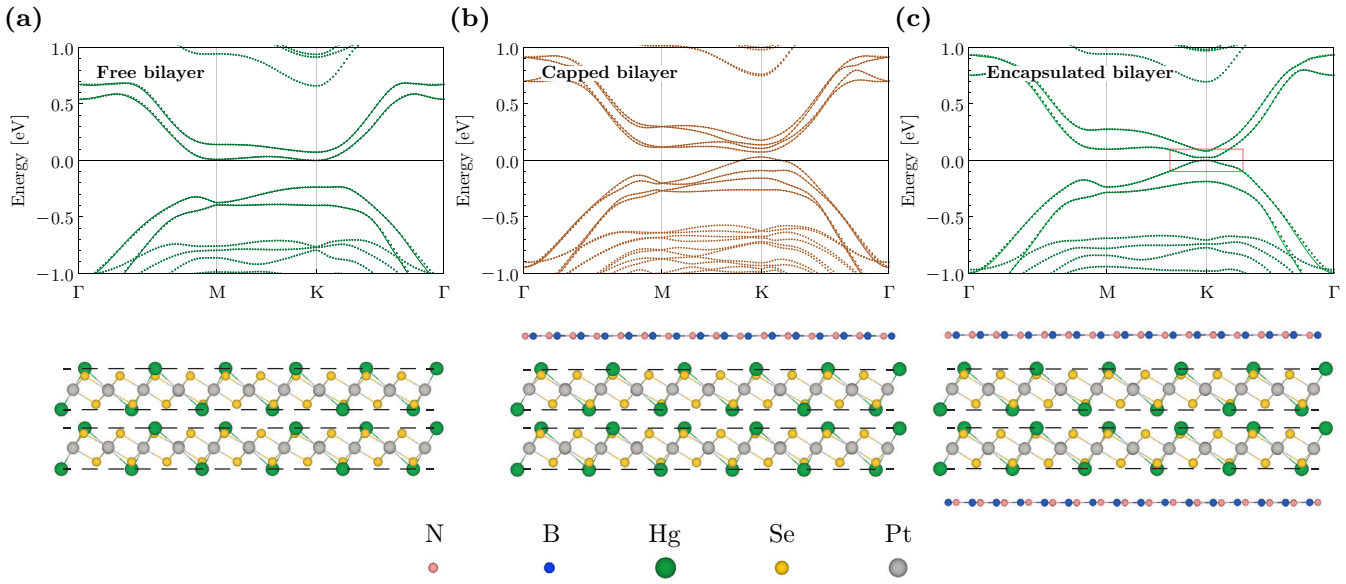

FIG. 1. Band structure and lateral view of the crystal structure for (a) free, (b) h-BN capped, and (c) h-BN encapsulated bilayer jacutingaite. In the top panels, the full band structure along the path **Γ**-**M**-**K**-**Γ** is shown with dots, while lines represent the Wannierized band structure of the eight bands closest to the Fermi level. The red rectangle in (c) highlights the region around the gap magnified in Fig. 2. In the bottom panels, we note that in each Pt_2HgSe_3 layer Hg atoms form a buckled honeycomb lattice [see also Fig. 3 for a top view in the case of (c)], with Hg atoms in the two sublattices alternating above and below a Pt_2Se_3 layer. Dashed lines highlight the vertical position of Hg planes, showing the inequivalence of inner and outer planes, the latter tending to extend farther away from the Pt_2Se_3 layer. This tendency, most apparent in the free bilayer, is suppressed by the presence of h-BN, with the encapsulated bilayer recovering a more symmetric structure of each layer.

drives bulk jacutingaite into a semimetallic state endowed with a dual topology [31–33] that combines a nonzero mirror Chern number with a weak topology. Recent experiments have verified both the semimetallic nature of bulk Pt_2HgSe_3 [34,35] and the presence of surface states protected by the crystalline mirror symmetry [36].

Here we consider bilayer jacutingaite and predict using first-principles simulations that it is trivial, although in an unexpected way, with $\nu_{bi} = 0 + 0$. The trivial gap arises from inversion-symmetry breaking in each layer, with competing contributions from a structural distortion and the different environments affecting intrasublattice hopping. As a result of this sublattice imbalance, the Kane-Mele term that drives the topological nature of monolayer jacutingaite [23] is replaced by a spin-orbit coupling that has the same sign on the two sublattices. When encapsulated in hexagonal boron nitride (h-BN), the trivial gap is strongly reduced and can be turned topological by a small perpendicular field, promoting bilayer Pt_2HgSe_3 into a promising system for experimental explorations.

II. BILAYER STRUCTURES

Jacutingaite comprises AA-stacked honeycomb lattices of Hg atoms, where the A (B) sublattice is positioned above (below) a plane of Pt atoms (see Fig. 1). In the absence of spin-orbit coupling, the electronic band structure of monolayer jacutingaite contains gapless Dirac cones at the corners **K** and **K**′ of the hexagonal Brillouin zone [23], which is similar to what happens in graphene. These cones can be gapped in two different ways. The first is by breaking the sublattice (inversion) symmetry, e.g., by making the Hg distance to the Pt planes different on the two sides, leading to a trivial insulator. The second way to open a gap is via Kane-Mele spin-orbit coupling, making monolayer jacutingaite a quantum spin Hall insulator.

In bilayer jacutingaite, although global inversion symmetry connecting the two layers is still present, there is no inversion symmetry *per layer*; that is, the two sublattices in each layer are no longer equivalent. This means that Hg atoms can be displaced to make each layer by itself trivial ($\nu_{bi} = 0 + 0 = 0$). If no or only small displacements occur and the two layers are almost independent, however, the combination of two topological monolayers together makes the bilayer trivial, following the heuristic rule $\nu_{bi} = 1 + 1 = 0$. In either case, bilayer jacutingaite is expected to be a trivial insulator.

To confirm this, we perform first-principles density-functional theory (DFT) calculations of various few-layered jacutingaite structures using QUANTUM ESPRESSO [37,38], with a Coulomb cutoff [39] to reproduce the correct open boundary conditions in the vertical direction and the van der Waals compliant functional vdw-DF-cx [40–42] that gives the best agreement with Raman experiments for the vibrational frequencies of bulk jacutingaite [34] (for further details of the calculations see Appendix A). The unit cell is hexagonal (point group D_{3d} or $\bar{3}m$) with the in-plane lattice constant fixed to the bulk relaxed value $a = 7.384$ Å.

We first relax the structure of a freestanding bilayer, which shows a large shift in the vertical position of the outer Hg atoms. The distance of the Hg atoms to the Pt planes increases from 1.73 Å in the monolayer to 2.02 Å for the outer Hg atoms. The sublattice asymmetry is responsible for a large trivial ($\nu_{bi} = 0 + 0 = 0$) band gap of 290 meV at the **K** point (see Appendix C and the discussion below). The same level

TABLE I. Main properties of various layered jacutingaite structures. The monolayer and bulk have been studied before [23,31]; here we show results for free, capped, and encapsulated bilayers, as well as for trilayer Pt_2HgSe_3 (see also Appendix B). The second column contains the gap at **K** obtained using approximate DFT (see Appendix A). The third column contains the z position of the Hg atoms relative to the nearest Pt plane (see Fig. 1). Notice that in the capped, encapsulated, and trilayer cases the position depends on the layer (abbreviated "l.").

System	Gap at **K** (meV)	Δz Hg-Pt (Å)
Bulk	<1	1.84
Monolayer	168	1.73
Bilayer	290	1.81 (inner Hg)
		2.02 (outer Hg)
BN/bilayer	44	1.78 (outer Hg, capped l.)
		1.80 (inner Hg, capped l.)
		1.78 (inner Hg, free l.)
		1.90 (outer Hg, free l.)
BN/bilayer/BN	27	1.80 (inner Hg)
		1.78 (outer Hg)
Trilayer	<1	1.84 (middle l.)
		1.81 (inner Hg, outer l.)
		2.02 (outer Hg, outer l.)

of displacement is found in trilayer jacutingaite (see also Appendix B); however, the trilayer is semimetallic owing to a large second-nearest-layer hopping between the outer layers, similar to what happens in the bulk [31]. See Table I for an overview of the Hg positions and band gaps of the different studied structures.

The band gap in free bilayer jacutingaite is so large that a topological transition cannot be obtained using reasonable perpendicular external electric fields (up to 1 V/Å), unlike monolayer jacutingaite, which has a transition at $E_{\text{ext}} = 0.36\,\text{V/Å}$. This is because the external electric field is never sufficient to reduce the sublattice asymmetry. We note in passing that these values do not correspond to a potential drop across the system (e.g., $E_{\text{ext}} = 1\,\text{V/Å}$ does not correspond to 1 V over 1 Å), as in first-principles simulations we can set only the external electric field (related to the dielectric displacement D through $E_{\text{ext}} = 4\pi D$) and not the total electric field as in experiments (through the gate voltages applied to electrodes on the two sides of the system).

A possible way to restore sublattice symmetry, and thus to make a topological transition more feasible, at least in one layer, is to suppress the lattice distortion by encapsulating one side of bilayer jacutingaite with h-BN. As can be seen in Table I and Fig. 1(b), this indeed reduces the sublattice asymmetry in one of the layers and reduces the gap. However, the system is still $0 + 0 = 0$ trivial, and fields up to 1 V/Å do not induce a topological transition; instead, they make the system metallic, with a charge transfer from the bilayer to h-BN.

On the other hand, the reduction in gap size suggests that fully encapsulating bilayer jacutingaite with h-BN might bring us to the regime where we can induce a topological transition via an electric field. We indeed find that the Hg positions are nearly symmetrical in h-BN encapsulated bilayers.

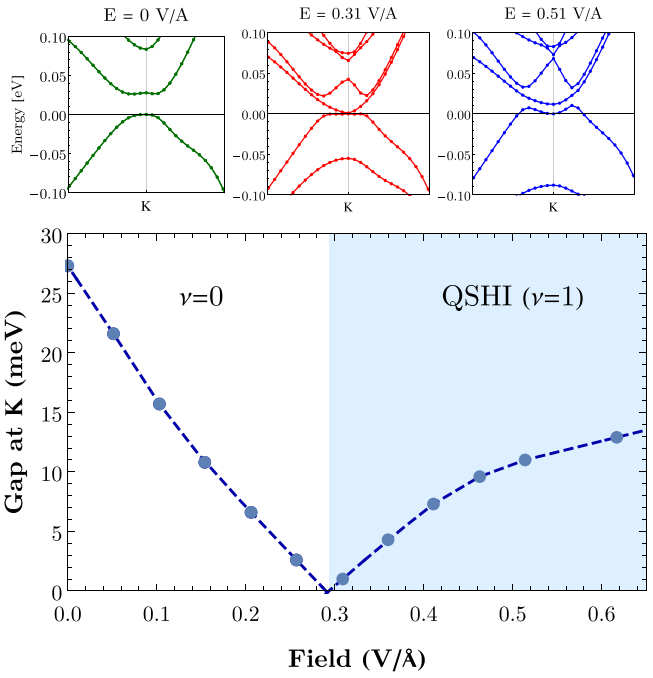

FIG. 2. Top: Band structure of h-BN encapsulated bilayer jacutingaite around the **K** point in a small energy window close to the Fermi energy for three different values of the applied external electric field. Note that at zero field all bands are doubly degenerate due to inversion symmetry, whereas at nonzero fields this degeneracy is lifted. Bottom: The direct gap at the **K** point as a function of perpendicular external electric field. Around $E_{\text{ext}} = 0.3\,\text{V/Å}$ the gap closes. For larger fields, a band inversion occurs, and the system is a quantum spin Hall insulator with $\nu = 1$. The indirect band gap is shown in Appendix D, while the direct gap computed with different functionals is reported in Appendix E.

Furthermore, the gap is reduced to only 27 meV, which brings us into the regime that allows for a topological transition.

III. BAND STRUCTURE AND WANNIERIZATION

We will now discuss in depth the properties of the encapsulated bilayer structure. For simplicity, we locate the h-BN layers on the two sides of the bilayer so that, in the absence of an external electric field, the total system again contains inversion symmetry, and we let only the vertical position of the h-BN layers relax. The full band structure is shown in the top panel of Fig. 1(c) for $E_{\text{ext}} = 0$, where all bands are doubly degenerate as a consequence of time-reversal and inversion symmetries. Whereas the bandwidth of the four main bands is about 1 eV, the band gap is only 27 meV (see the top left panel of Fig. 2 for a closer look at the band structure around **K** near the Fermi energy).

When a finite external electric field E_{ext} is applied, the gap at **K** reduces, until it closes at about $E_{\text{ext}} = 0.3\,\text{V/Å}$, as shown in the top middle panel of Fig. 2. At larger fields, the gap reopens and increases with E_{ext}, with bands at **K** that are inverted, as shown in the top right panel of Fig. 2 for $E_{\text{ext}} = 0.5\,\text{V/Å}$. The full dependence of the direct gap size at **K** as a function of external electric field is reported in the bottom panel of Fig. 2. It is important to stress that the

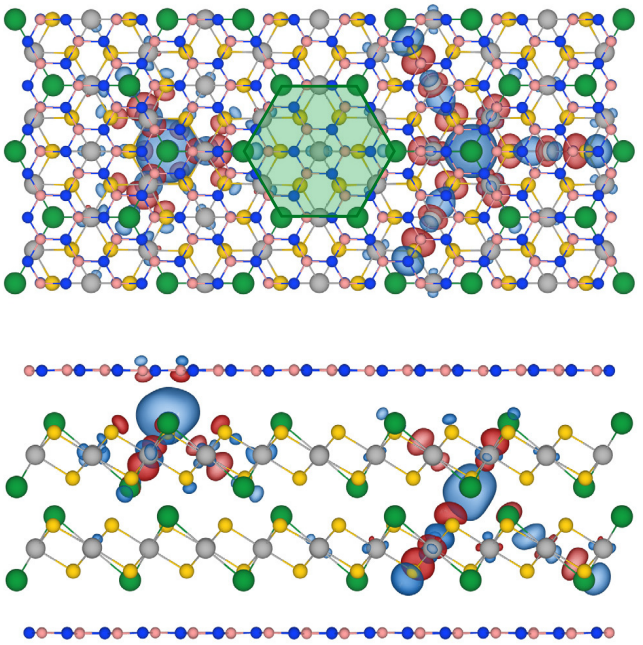

FIG. 3. Top and lateral views of the crystal structure of h-BN encapsulated bilayer jacutingaite. In the top view, the green shaded area highlights the hexagonal Wigner-Seitz unit cell and the (buckled) honeycomb lattice formed by Hg atoms. Two Wannier functions associated with the two sublattices of the upper layer are also reported as isosurfaces for both positive (blue) and negative (red) values. The Wannier functions associated with the bottom layer can be simply obtained by inversion symmetry.

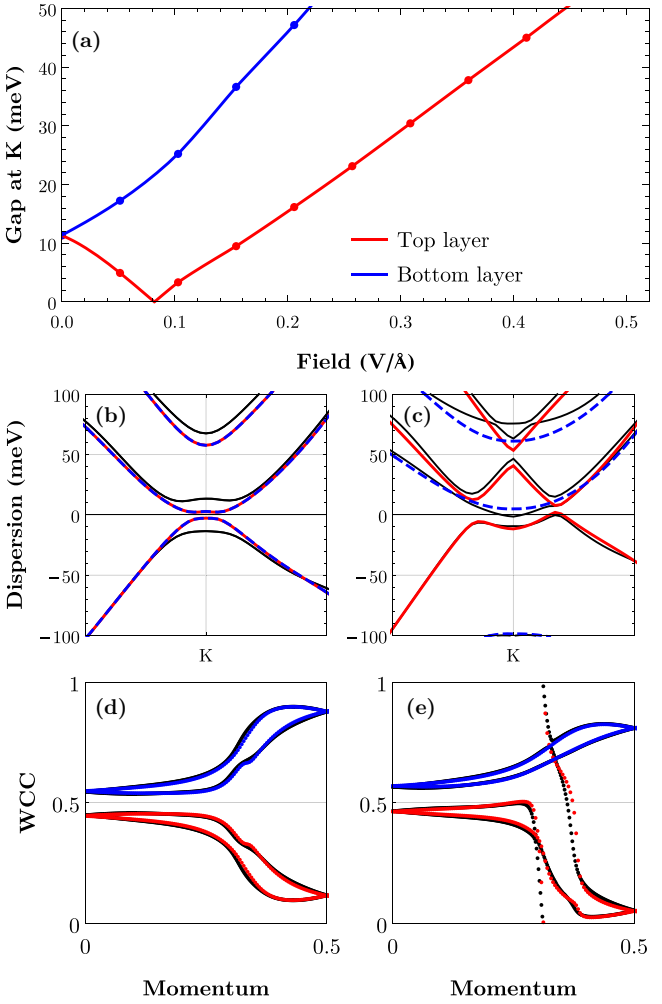

FIG. 4. Bilayer jacutingaite can be qualitatively understood as two decoupled layers. (a) To verify this, we calculated the gap at **K** as a function of external field for the individual layers using the tight-binding model with interlayer couplings set to zero. Though the gap is quantitatively underestimated (compare with Fig. 2), we still find a topological transition in the top layer. (b) The dispersion close to **K** changes only subtly when we have interlayer coupling (black solid lines) or not (red and blue dashed lines) at zero field. (c) At a finite external field of $E_{\text{ext}} = 0.46\,\text{V/Å}$, the dispersion for just the top layer (red) and bottom layer (blue) still has a large overlap with the full bilayer band structure. (d) The WCCs (in units of the lattice parameter a) computed for the full tight-binding model (black) are the same as the WCCs computed per layer (red and blue). (e) Same calculation as in (d), but now at a finite field $E_{\text{ext}} = 0.46\,\text{V/Å}$. We clearly see the topological nature of the bands in the top layer (red).

calculated value of the critical field at which the topological transition occurs might depend on the choice of approximate DFT and the corresponding evolution of the energy gap with E_{ext}. Moreover, since approximate semilocal DFT typically tends to underestimate energy gaps with respect to experiments, the critical field might be severely underestimated. To test the reliability of the above predictions we have thus performed hybrid-functional calculations, which are expected to provide more realistic estimates of the energy band gap [43] (see Appendix E). The semilocal and hybrid-functional estimates give a good approximation of the lower and upper bounds of the critical field E_{ext}, which should be compared with experimental results.

To elucidate whether the band inversion is associated with a topological phase transition, we map first-principles eigenstates for the bands facing the energy gap into a set of maximally localized Wannier functions (WFs) [44] using WANNIER90 [45]. The Hg s orbitals are used as first projections to initialize the Wannierization procedure, as in the case of monolayer [23] and bulk [31] Pt_2HgSe_3. We thus end up with four WFs (eight by including spin), two per layer, which are depicted in Fig. 3 for the top layer when $E_{\text{ext}} = 0$. While for the external sublattice the WF is similar to that of the monolayer [23] and it is well localized on just one layer, the inner WF has significant contributions from orbitals in the opposite layer, signaling a strong hybridization between the layers similar to what happens in bulk jacutingaite [31]. As a result, the center of the inner WFs is significantly shifted in the z direction such that the center of the top WF of the bottom layer is *higher* than that of the bottom WF of the top layer.

From the knowledge of the WFs, we can easily compute the $\mathbb{Z}_2$ topological invariant using WANNIERTOOLS [46] by monitoring the evolution of the Wannier charge centers (WCCs) over half of the Brillouin zone [47,48], i.e., the expectation value of the coordinate along one direction of hybrid WFs [49] as a function of momentum in the remaining direction, along which they are delocalized. The $\mathbb{Z}_2$ invariant ν can

TABLE II. Dominant tight-binding parameters of the band structure of encapsulated bilayer jacutingaite, obtained using WANNIER90. The first column indicates the type of coupling; the second column indicates how it acts on spin (s), sublattice (σ), and layer (τ) spaces. NN stands for nearest neighbor, and NNN stands for next-nearest neighbor. Notice that the NNN Rashba and Kane-Mele spin-orbit coupling terms are highly imbalanced between the two sublattices.

Coupling	Proportional to	Value (meV)
On-site potential m	$\sigma^z\tau^z$	135
NN intralayer t	$\sigma^{x,y}$	233
NN Rashba λ_R	$s^{x,y}\sigma^{x,y}\tau^z$	10
NN interlayer t_1	$\sigma^{x,y}\tau^{x,y}$	53
NNN intralayer t_2	$(1-\sigma^z\tau^z)$	−34 (outer)
	$(1+\sigma^z\tau^z)$	32 (inner)
NNN Rashba λ_R'	$s^{x,y}(\sigma^z-\tau^z)$	28 (outer only)
NNN Kane-Mele λ_{KM}	$\sigma^z s^z(1-\sigma^z\tau^z)$	16 (outer)
	$\sigma^z s^z(1+\sigma^z\tau^z)$	−2 (inner)
NNN interlayer t_2'	$\tau^{x,y}$	−20

then be obtained by considering the parity of the number of times an arbitrary curve going from $k=0$ to $k=0.5$ (in units of the primitive reciprocal lattice vector in that direction) crosses the WCC lines [47,48]. As shown in Fig. 2, this confirms the presence of a topological transition as a function of the external electric field [see Figs. 4(d) and 4(e) for the WCC evolution at small and large fields]. In particular, while the system is trivial ($\nu=0$) in the absence of external fields (confirmed also using a parity approach [50]), it becomes a QSHI ($\nu=1$) when $E_{\mathrm{ext}} > 0.3\,\mathrm{V/Å}$, showing that the topological state of bilayer jacutingaite can easily be manipulated.

The mapping of the first-principles results into WFs can be beneficial also for extracting an effective tight-binding model that describes the behavior of bilayer jacutingaite, helping us to gain additional physical insight into the mechanisms underlying the topological transition. The resulting eight-band model (including spin) reproduces the DFT band structure around the band gap (see Fig. 1) and involves the sites of two buckled honeycomb lattices—one for each layer—with one orbital per site and spin (given by the WFs in Fig. 3). We find that even though the WFs associated with the inner sublattices are delocalized over the two layers (see Fig. 3 and the discussion above), the effective tight-binding model is still dominated by intralayer terms.

In Table II we summarize the most important terms of the effective tight-binding model when $E_{\mathrm{ext}}=0$. The two largest contributions are by far the intralayer nearest-neighbor (NN) hopping $t=233\,\mathrm{meV}$ and the sublattice symmetry breaking on-site term $m=135\,\mathrm{meV}$. The absence of layer-inversion symmetry allows a NN (Rashba-like) spin-orbit coupling λ_R that is vanishing in isolated monolayers.

The most important contribution that couples the two layers is a NN hopping $t_1\sim 50\,\mathrm{meV}$, which, together with the other relevant interlayer term t_2' in Table II, plays a minor role in the band structure. To verify this, we calculated the band structure using the full tight-binding model with and without interlayer coupling. The result is shown in Fig. 4. In the absence of a perpendicular field, the band- structure is marginally changed: removing the interlayer coupling mainly reduces the gap at **K**. The interlayer coupling can therefore be neglected for a qualitative understanding of the topological transition.

An external field now reduces the gap further in the top layer, whereas it increases the gap in the bottom layer (Fig. 4). This behavior is indicative of the topological transition that goes from a $\nu=0+0$ to $\nu=0+1$ state. Indeed, Fig. 4(d) [Fig. 4(e)] shows the evolution of the WCCs at small (large) external field. In both cases the WCCs of the full model (black) are consistent with the WCC computed for the separate layers (blue and red), thus justifying the assumption that the topological invariant can be expressed as the sum of the invariants in the two layers, $\nu_{\mathrm{bi}}=\nu_1+\nu_2$. Moreover, while for small fields both layers are trivial (and related by inversion symmetry), for large fields the layers are no longer equivalent, and the top layer (red) is nontrivial after the gap reopens at **K**.

Within each layer, the inequivalence of the two sublattices not only makes the on-site energy very different (as expressed by m) but also introduces a large imbalance in the intralayer next-nearest-neighbor (NNN) hopping terms. It arises as a result of the different (de)localizations of the Wannier orbitals for the inner and outer sublattice sites. A first important example of the NNN term is the hopping energy t_2 that takes approximately opposite values for the inner and outer sublattices. In particular, we find that t_2 is positive for the outer sites, similar to what happens in monolayer Pt_2HgSe_3, while it is negative for inner sites, in complete analogy with bulk jacutingaite. This effectively *staggered* NNN hopping term gives rise to a trivial gap at **K** that is found to compete with the trivial gap associated with the on-site m (see also below). This compensation is almost perfect in h-BN encapsulated bilayers (contrary to the freestanding case), thus explaining the very small trivial gap at **K**.

Even more compelling, the imbalance affects also two additional NNN spin-orbit terms: Kane-Mele [9,10] and in-plane Rashba-like [51] spin-orbit couplings. Also in this case, these terms retain values very close to the one in the monolayer for the outer sublattices [23,25,52], while they are strongly suppressed for the inner sublattices, in analogy with bulk jacutingaite, where the effect of spin-orbit coupling is almost negligible [31–33]. Traditionally, topological transitions were understood in terms of spin-orbit couplings that were identical on both sublattices [9,10]. In bilayer jacutingaite, however, the fact that the spin-orbit coupling is different on the two sublattices requires an extension of the original Kane-Mele model.

IV. IMBALANCED KANE-MELE MODEL

As argued in the previous section, the topological transition can be qualitatively understood by decoupling the two layers and focusing on only the top layer. We will now explore the question of whether we can understand the transition purely in terms of a short-range hopping model. To this end, we introduce the so-called *imbalanced Kane-Mele* model, which contains nearest (t) and staggered next-nearest-neighbor (t_2) hoppings, a sublattice symmetry-breaking potential m, and *two* spin-orbit terms (see Fig. 5). In addition to the regular Kane-Mele (KM) term $i\lambda_{\mathrm{KM}}\sum_{\langle\langle ij\rangle\rangle}\nu_{ij}c_i^\dagger s^z c_j$, which has opposite signs on the two sublattices, we include a *sublattice-*

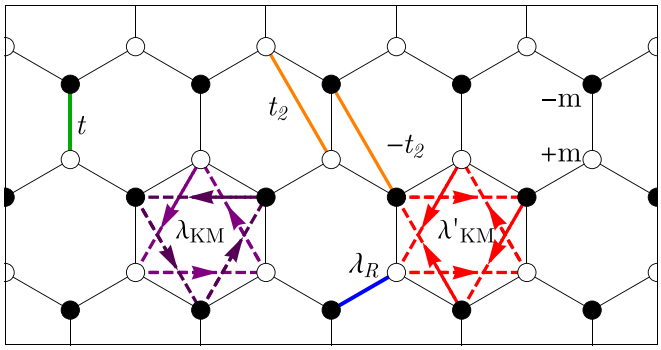

FIG. 5. Terms in the imbalanced Kane-Mele model. We include nearest-neighbor hopping t and next-nearest-neighbor hopping t_2. Sublattice symmetry breaking is included by the term $m\sigma^z$. The spin-orbit terms include the regular Kane-Mele term $\lambda_{KM}\sigma^z s^z$ and a *sublattice-symmetric Kane-Mele term* $\lambda'_{KM}s^z$. The arrow directions indicate the sign of the imaginary hopping. Finally, we include a nearest-neighbor Rashba term λ_R that stabilizes an unusual topological insulator phase when $\lambda'_{KM} > \lambda_{KM}$.

symmetric Kane-Mele term λ'_{KM},

$$i\lambda'_{KM}\sum_{\langle\langle ij\rangle\rangle}\nu_{ij}c_i^\dagger\sigma^z s^z c_j. \quad (1)$$

This term, as shown in Fig. 5, has the *same sign* of the spin-orbit coupling term on the two sublattices. As a consequence, the effective spin-orbit coupling on the two sublattices is given by $\lambda_{KM} \pm \lambda'_{KM}$.

In momentum space, the regular KM term is proportional to $\lambda_{KM}d(\mathbf{k})\sigma^z s^z$, where $d(\mathbf{k}) = 2\sin(k_x a) - 4\sin(k_x a/2)\cos(\sqrt{3}k_y a/2)$ [10], if we define the honeycomb lattice with lattice vectors $\mathbf{a}_{1,2} = \frac{a}{2}(\pm 1, \sqrt{3})$. Consequently, the sublattice-symmetric KM term is proportional to $\lambda'_{KM}d(\mathbf{k})s^z$. As a result, at the $\mathbf{K}$ and $\mathbf{K}'$ points, the Hamiltonian reads

$$H = (m - 3t_2)\sigma^z + 3\sqrt{3}\lambda_{KM}\kappa\sigma^z s^z + 3\sqrt{3}\lambda'_{KM}\kappa s^z, \quad (2)$$

where $\kappa = \pm 1$ for the $\mathbf{K}/\mathbf{K}'$ valley. In the absence of spin-orbit coupling, the trivial gap at $\mathbf{K}$ is determined by the sublattice potential reduced by the staggered nearest-neighbor hopping, $m - 3t_2$. For $\lambda_{KM} > \lambda'_{KM} > 0$, the gap is insensitive to the sublattice-symmetric KM term and is given by $\Delta = |m - 3t_2| - 3\sqrt{3}\lambda_{KM}$. As long as this parameter Δ is positive, the system is trivial, and for $\Delta < 0$ the model is a quantum spin Hall insulator with $\nu = 1$. When the two spin-orbit terms are exactly equal, $\lambda_{KM} = \lambda'_{KM}$, the system realizes a semimetal with quadratic band touching as long as $\Delta < 0$. If the sublattice-symmetric KM term dominates, $\lambda_{KM} < \lambda'_{KM}$, the system is either metallic ($\Delta' < 0$) or a trivial insulator ($\Delta' > 0$), with $\Delta' = |m - 3t_2| - 3\sqrt{3}\lambda'_{KM}$.

When the NN Rashba spin-orbit coupling

$$i\lambda_R\sum_{\langle ij\rangle}c_i^\dagger(\mathbf{s}\times\mathbf{d}_{ij})^z c_j \quad (3)$$

(arising from the inversion symmetry breaking in each layer) is also included, not only is a finite gap opened in the semimetallic phase when $\lambda_{KM} < \lambda'_{KM}$, but also a nontrivial topological state emerges for $m - 3t_2 < \lambda'_{KM}$. When $m - 3t_2$ further decreases, the gap closes again (away from $\mathbf{K}/\mathbf{K}'$ at three Dirac cones around each corner of the Brillouin zone), and the system enters a trivial phase adiabatically connected to the one for $\Delta' > 0$ when $\lambda_R = 0$. The topological phase thus survives over a finite interval of values of $m - 3t_2$, whose extension increases with λ_R and is nonvanishing only when $m - 3t_2$ has the same sign as λ'_{KM}, even in the limit $\lambda_{KM} \to 0$.

From Table II it follows that in bilayer jacutingaite the sublattice-symmetric KM term dominates: $\lambda'_{KM} = 9$ meV, while $\lambda_{KM} = 7$ meV (their sum is the "outer" sublattice Kane-Mele term, while their difference is the inner one). In the absence of a field, the sublattice potential m controls the physics, and we expect a trivial insulator. A perpendicular electric field affects the value of m and t_2 because of the different z positions of the Wannier orbitals. In particular, by Wannierizing the electronic structure at different E_{ext}, we find that the on-site potential and the staggered hopping t_2 change linearly with field, approximately as $\Delta m = -135$ meV Å V^{-1} and $\Delta t_2 = 9$ meV Å V^{-1}. This change has opposite signs in the two layers, causing the bottom layer to have a larger trivial gap upon the application of a field, whereas the top layer reduces the gap.

Consistent with the results above, the imbalanced Kane-Mele model thus predicts that the bottom layer remains trivial with just an increasing gap at $\mathbf{K}$, while in the top layer the gap decreases and closes at a critical value when the field is such that $m - 3t_2 = \lambda'_{KM}$, in qualitative agreement with Fig. 4(a). When E_{ext} is further increased, the gap reopens, and the top layer is in a topologically nontrivial state ($\nu = 1$), protected by the NN Rashba λ_R. This prediction is validated by the fact that without spin-flipping intersublattice hopping terms (such as λ_R), no topological transition occurs even in the full WF tight-binding model. Of course, longer-range and interlayer hopping terms in the full model play a role in the quantitative determination of energy gaps and transition fields, but the imbalanced Kane-Mele is sufficient to describe the essential physical features of the topological transition occurring in encapsulated bilayer jacutingaite.

V. OUTLOOK

We predict that h-BN encapsulated bilayer Pt_2HgSe_3 undergoes a topological transition under the application of an electric field, from a trivial insulator at zero field to a quantum spin Hall insulator. The transition can be qualitatively understood by considering the layers decoupled and described by an imbalanced Kane-Mele model, with a new, sublattice-symmetric next-nearest-neighbor spin-orbit coupling. This additional term emerges from the inversion-symmetry breaking in each layer associated with the inequivalence of the two sublattices. This imbalance also allows for a nonzero Rashba spin-orbit coupling that plays an essential role in stabilizing the topological phase in large fields.

Jacutingaite has been predicted to be potentially exfoliable [23,26], and consequently, bilayer jacutingaite can also appear during an exfoliation process. Recently, experiments have shown that this is possible [29], although the quality of the exfoliated samples needs to be improved. If encapsulated,

exfoliated bilayer jacutingaite lead to the construction of a gate-switchable topological insulator (off at zero field, on at finite field), which is complementary to the monolayer case (on at zero field, off at finite field) [23].

ACKNOWLEDGMENTS

We greatly acknowledge A. Marrazzo for fruitful discussions. Support has been provided by the Swiss National Science Foundation (SNSF) through the Ambizione program (M.G.: Grant No. PZ00P2_174056, L.R.: Grant No. PZ00P2_174208). M.G. acknowledges support also from the Italian Ministry for University and Research through the Levi-Montalcini program and from the NCCR MARVEL funded by the SNSF. Simulation time was provided by the Swiss National Supercomputing Centre (CSCS) on Piz Daint (Production Project No. s917).

APPENDIX A: CALCULATION DETAILS

As mentioned in the main text, all first-principles DFT calculations were performed using the QUANTUM ESPRESSO suite of codes [37,38]. Structural relaxations were carried out using the cx variant [41] of the van der Waals compliant vdw-DF [40,42] functional without spin-orbit coupling, with pseudopotentials from the Standard Solid State Pseudopotential library [53] (efficiency version 1.0), with an energy cutoff of 60 Ry for wave functions and 480 Ry for the density. The Brillouin zone was sampled with $8 \times 8 \times 1$ k points of a uniform Γ-centered Monkhorst-Pack grid with a cold smearing of 0.015 Ry [54]. Band structures were computed by including spin-orbit coupling through fully relativistic pseudopotentials of the PSEUDODOJO family [55] with a wave function cutoff of 80 Ry on top of self-consistent calculations with $12 \times 12 \times 1$ k points within the generalized gradient approximation as formulated by Perdew, Burke, and Ernzerhof (PBE) [56]. Calculations with the Heyd-Scuseria-Ernzerhof (HSE) hybrid functional [57] have been performed with norm-conserving pseudopotentials [58] from the SG15 library [59,60] that do not have nonlinear core corrections, using a cutoff of 50 Ry both for wave functions and the representation of the Fock operator, and a 6×6 k-point grid.

Crystal structures and Wannier functions are visualized using VESTA [61].

APPENDIX B: TRILAYER CRYSTAL AND BAND STRUCTURE

Although the main target is bilayer jacutingaite, we have also considered the trilayer structure. In Fig. 6 we show both the relaxed crystal structure and the computed electronic band structure along a high-symmetry path in the Brillouin zone. We note that in contrast to the bilayer cases shown in Fig. 1, the system is metallic, mainly due to strong interlayer coupling between the outermost layers that is similar to the second-nearest-layer hopping of bulk jacutingaite [31].

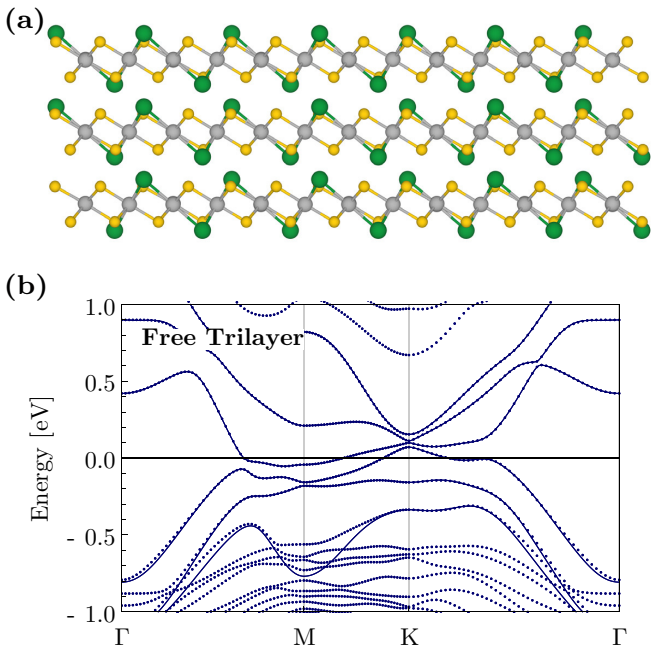

FIG. 6. (a) Lateral view of the crystal structure of free trilayer jacutingaite. The central layer is symmetric, while in the other layers the outermost Hg atoms are farther away from the central plane of Pt atoms with respect to the inner ones. (b) Electronic band structure of trilayer jacutingaite, where symbols represent direct calculations, while lines are the result of a minimal tight-binding model based on Wannier functions. The zero of energy is set at the Fermi level.

APPENDIX C: WANNIER CHARGE CENTERS FOR FREE AND CAPPED BILAYERS

In the main text we introduced in addition to the encapsulated bilayer jacutingaite a free bilayer and a h-BN capped bilayer (with h-BN only on one side), whose band structure is shown in Fig. 1. In Fig. 7 we plot the evolution of the Wannier charge centers to show that the free and capped bilayers are topologically trivial. In particular, the Wannier charge centers computed assuming the layers are decoupled (red and blue) are the same as for the full system (black), suggesting that the topological invariant for the bilayer can be expressed as the

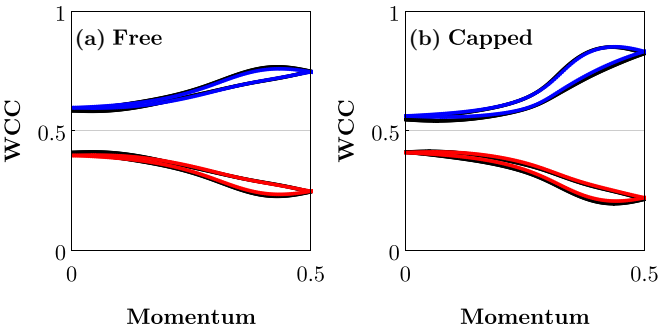

FIG. 7. Evolution of Wannier charge centers (WCCs) for (a) free and (b) h-BN capped bilayer Pt_2HgSe_3. Both systems are topologically trivial. Note that the WCCs (in units of the lattice parameter a) computed for the full tight-binding model (black) are the same as the WCCs computed per layer (red and blue).

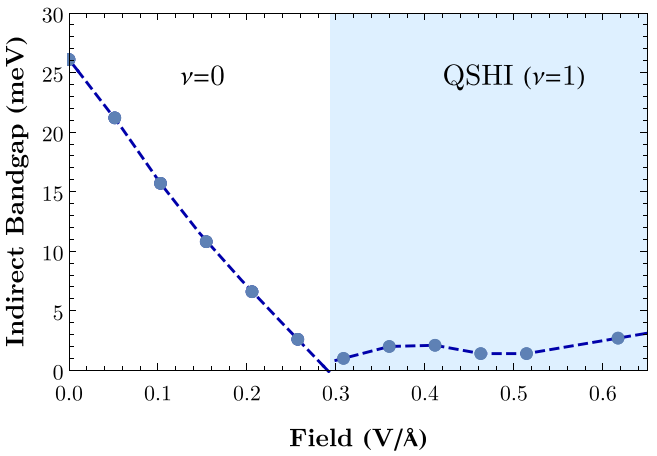

FIG. 8. The indirect band gap (measured as the minimum of the conduction band minus the maximum of the valence band) of the encapsulated bilayer as a function of external electric field. In the topological phase the gap is smaller than the direct gap at **K** in Fig. 2 but still positive, suggesting the presence of a fully developed band gap.

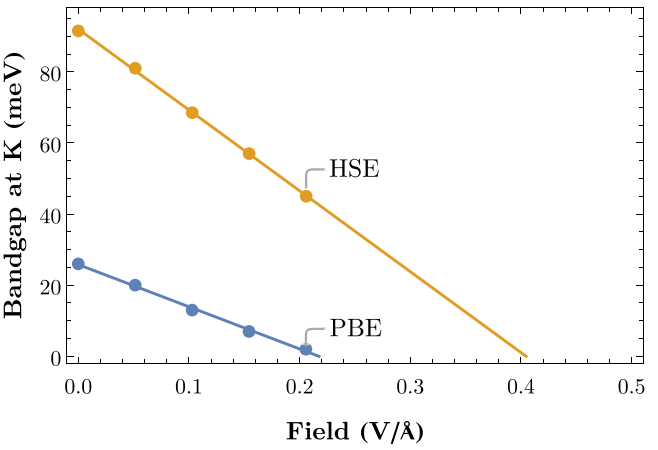

FIG. 9. Direct band gap at the **K** point for h-BN encapsulated bilayer jacutingaite as a function of the external electric field computed using either the PBE [56] or the HSE [57] functional. Dots represent actual calculation results, while lines are linear extrapolations.

sum of the invariants of the two layers, $\nu_{\rm bi} = \nu_1 + \nu_2$, with $\nu_1 = \nu_2 = 0$.

APPENDIX D: INDIRECT GAP IN THE ENCAPSULATED BILAYER

In the topological phase, the direct gap at **K** of the encapsulated bilayer in Fig. 2 is not equal to the full band gap. This is typical for band inversion and is visible in the band structure of Fig. 2. Nevertheless, the maximum of the valence band remains below the minimum of the conduction band; that is, there is a fully developed band gap, whose magnitude is shown in Fig. 8.

APPENDIX E: DIRECT GAP WITH A HYBRID FUNCTIONAL

Standard approximations to DFT, including the generalized gradient PBE approximation [56] used here (see Appendix A), tend to largely underestimate the energy gap, so that topological transitions and the corresponding critical electric field might also be affected. To test the reliability of the conclusions in the main text, we report here results for the direct gap at **K** (which controls the topological transition) of the encapsulated bilayer using hybrid functionals (in particular the HSE functional [57]), which typically lead to estimates of the energy gap in closer agreement with experiments [43].

Figure 9 shows that for $E_{\rm ext} = 0$ the gap is largely underestimated by almost a factor of 4 in PBE-DFT with respect to hybrid-functional calculations. Still, the rate at which the gap closes as a function of the external electric field is much larger with the HSE functional than with PBE (note that the latter results slightly differ from Fig. 2 because smearing is not used in this case and thus the almost linear behavior extends down to zero gap while deviations associated with smearing appear in Fig. 2). As a consequence, a topological phase transition still occurs even at the HSE level, and the estimated critical field is only a factor of 2 larger than in PBE calculations, supporting the robustness of the phenomena discussed in the main text.

[1] M. Z. Hasan and C. L. Kane, Colloquium: Topological insulators, Rev. Mod. Phys. **82**, 3045 (2010).
[2] B. A. Bernevig and T. L. Hughes, *Topological insulators and topological superconductors* (Princeton University Press, Princeton, NJ, 2013).
[3] A. Kitaev, Periodic table for topological insulators and superconductors, in Advances in Theoretical Physics: Landau Memorial Conference, *AIP Conf. Proc.* No. 1134 (AIP, Melville, NYU, 2009), p. 22.
[4] S. Ryu, A. P. Schnyder, A. Furusaki, and A. W. W. Ludwig, Topological insulators and superconductors: Tenfold way and dimensional hierarchy, New J. Phys. **12**, 065010 (2010).
[5] L. Fu, Topological Crystalline Insulators, Phys. Rev. Lett. **106**, 106802 (2011).
[6] R.-J. Slager, A. Mesaros, V. Juričić, and J. Zaanen, The space group classification of topological band-insulators, Nat. Phys. **9**, 98 (2013).
[7] D. J. Thouless, M. Kohmoto, M. P. Nightingale, and M. den Nijs, Quantized Hall Conductance in a Two-Dimensional Periodic Potential, Phys. Rev. Lett. **49**, 405 (1982).
[8] M. Kohmoto, Topological invariant and the quantization of the Hall conductance, Ann. Phys. (NY) **160**, 343 (1985).
[9] C. L. Kane and E. J. Mele, Quantum Spin Hall Effect in Graphene, Phys. Rev. Lett. **95**, 226801 (2005).
[10] C. L. Kane and E. J. Mele, $\mathbb{Z}_2$ Topological Order and the Quantum Spin Hall Effect, Phys. Rev. Lett. **95**, 146802 (2005).
[11] B. A. Bernevig and S.-C. Zhang, Quantum Spin Hall Effect, Phys. Rev. Lett. **96**, 106802 (2006).

[12] B. A. Bernevig, T. L. Hughes, and S.-C. Zhang, Quantum spin Hall effect and topological phase transition in HgTe quantum wells, Science **314**, 1757 (2006).

[13] M. König, S. Wiedmann, C. Brüne, A. Roth, H. Buhmann, L. W. Molenkamp, X.-L. Qi, and S.-C. Zhang, Quantum spin Hall insulator state in HgTe quantum wells, Science **318**, 766 (2007).

[14] A. Roth, C. Brüne, H. Buhmann, L. W. Molenkamp, J. Maciejko, X.-L. Qi, and S.-C. Zhang, Nonlocal transport in the quantum spin Hall state, Science **325**, 294 (2009).

[15] G. Grabecki, J. Wróbel, M. Czapkiewicz, L. Cywiński, S. Gieraltowska, E. Guziewicz, M. Zholudev, V. Gavrilenko, N. N. Mikhailov, S. A. Dvoretski, F. Teppe, W. Knap, and T. Dietl, Nonlocal resistance and its fluctuations in microstructures of band-inverted HgTe/(Hg,Cd)Te quantum wells, Phys. Rev. B **88**, 165309 (2013).

[16] M. König, M. Baenninger, A. G. F. Garcia, N. Harjee, B. L. Pruitt, C. Ames, P. Leubner, C. Brüne, H. Buhmann, L. W. Molenkamp, and D. Goldhaber-Gordon, Spatially Resolved Study of Backscattering in the Quantum Spin Hall State, Phys. Rev. X **3**, 021003 (2013).

[17] I. Knez, R. R. Du, and G. Sullivan, Evidence for Helical Edge Modes in Inverted InAs/GaSb Quantum Wells, Phys. Rev. Lett. **107**, 136603 (2011).

[18] K. Suzuki, Y. Harada, K. Onomitsu, and K. Muraki, Edge channel transport in the InAs/GaSb topological insulating phase, Phys. Rev. B **87**, 235311 (2013).

[19] Z. Fei, T. Palomaki, S. Wu, W. Zhao, X. Cai, B. Sun, P. Nguyen, J. Finney, X. Xu, and D. H. Cobden, Edge conduction in monolayer WTe_2, Nat. Phys. **13**, 677 (2017).

[20] S. Tang *et al.*, Quantum spin Hall state in monolayer $1T' - WTe_2$, Nat. Phys. **13**, 683 (2017).

[21] S. Wu, V. Fatemi, Q. D. Gibson, K. Watanabe, T. Taniguchi, R. J. Cava, and P. Jarillo-Herrero, Observation of the quantum spin Hall effect up to 100 kelvin in a monolayer crystal, Science **359**, 76 (2018).

[22] Y. Shi, J. Kahn, B. Niu, Z. Fei, B. Sun, X. Cai, B. A. Francisco, D. Wu, Z.-X. Shen, X. Xu, D. H. Cobden, and Y.-T. Cui, Imaging quantum spin Hall edges in monolayer WTe_2, Sci. Adv. **5**, eaat8799 (2019).

[23] A. Marrazzo, M. Gibertini, D. Campi, N. Mounet, and N. Marzari, Prediction of a Large-Gap and Switchable Kane-Mele Quantum Spin Hall Insulator, Phys. Rev. Lett. **120**, 117701 (2018).

[24] F. Luo, X. Hao, Y. Jia, J. Yao, Q. Meng, S. Zhai, J. Wu, W. Dou, and M. Zhou, Functionalization induced quantum spin Hall to quantum anomalous Hall phase transition in monolayer jacutingaite, Nanoscale **13**, 2527 (2021).

[25] Z. Liu, Y. Han, Y. Ren, Q. Niu, and Z. Qiao, Van der Waals heterostructure Pt_2HgSe_3/CrI_3 for topological valleytronics, arXiv:2012.13298.

[26] N. Mounet, M. Gibertini, P. Schwaller, D. Campi, A. Merkys, A. Marrazzo, T. Sohier, I. E. Castelli, A. Cepellotti, G. Pizzi, and N. Marzari, Two-Dimensional Materials from High-Throughput Computational Exfoliation of Experimentally Known Compounds, Nat. Nanotechnol. **13**, 246 (2018).

[27] A. R. Cabral, H. F. Galbiatti, R. Kwitko-Ribeiro, and B. Lehmann, Platinum enrichment at low temperatures and related microstructures, with examples of hongshiite (PtCu) and empirical 'Pt_2HgSe_3' from Itabira, Minas Gerais, Brazil, Terra Nova **20**, 32 (2008).

[28] A. Vymazalová, F. Laufek, M. Drábek, A. R. Cabral, J. Haloda, T. Sidorinová, B. Lehmann, H. F. Galbiatti, and J. Drahokoupil, Jacutingaite, Pt_2HgSe_3, a new platinum-group mineral species from the Cauê iron-ore deposit, Itabira district, Minas Gerais, Brazil, Can. Mineral. **50**, 431 (2012).

[29] K. Kandrai, G. Kukucska, P. Vancsó, J. Koltai, G. Baranka, Z. E. Horváth, Á. Hoffmann, A. Vymazalová, L. Tapasztó, and P. Nemes-Incze, Signature of large-gap quantum spin Hall state in the layered mineral jacutingaite, Nano Lett. **20**, 5207 (2020).

[30] L. Fu, C. L. Kane, and E. J. Mele, Topological Insulators in Three Dimensions, Phys. Rev. Lett. **98**, 106803 (2007).

[31] A. Marrazzo, N. Marzari, and M. Gibertini, Emergent dual topology in the three-dimensional Kane-Mele Pt_2HgSe_3, Phys. Rev. Res. **2**, 012063(R) (2020).

[32] J. I. Facio, S. K. Das, Y. Zhang, K. Koepernik, J. van den Brink, and I. C. Fulga, Dual topology in jacutingaite Pt_2HgSe_3, Phys. Rev. Mater. **3**, 074202 (2019).

[33] B. Ghosh, S. Mardanya, B. Singh, X. Zhou, B. Wang, T.-R. Chang, C. Su, H. Lin, A. Agarwal, and A. Bansil, Saddle-point Van Hove singularity and dual topological state in Pt_2HgSe_3, Phys. Rev. B **100**, 235101 (2019).

[34] D. Mauro, H. Henck, M. Gibertini, M. Filippone, E. Giannini, I. Gutiérrez-Lezama, and A. F. Morpurgo, Multi-frequency Shubnikov-de Haas oscillations in topological semimetal Pt_2HgSe_3, 2D Mater. **7**, 025042 (2020).

[35] C. Pei, S. Jin, P. Huang, A. Vymazalova, L. Gao, Y. Zhao, W. Cao, C. Li, P. Nemes-Incze, Y. Chen, H. Liu, G. Li, and Y. Qi, Pressure-induced superconductivity in dual-topological semimetal Pt_2HgSe_3, arXiv:2102.08801.

[36] I. Cucchi, A. Marrazzo, E. Cappelli, S. Riccò, F. Y. Bruno, S. Lisi, M. Hoesch, T. K. Kim, C. Cacho, C. Besnard, E. Giannini, N. Marzari, M. Gibertini, F. Baumberger, and A. Tamai, Bulk and Surface Electronic Structure of the Dual-Topology Semimetal Pt_2HgSe_3, Phys. Rev. Lett. **124**, 106402 (2020).

[37] P. Giannozzi *et al.*, QUANTUM ESPRESSO: A modular and open-source software project for quantum simulations of materials, J. Phys.: Condens. Matter **21**, 395502 (2009).

[38] P. Giannozzi *et al.*, Advanced capabilities for materials modeling with QUANTUM ESPRESSO, J. Phys.: Condens. Matter **29**, 465901 (2017).

[39] T. Sohier, M. Calandra, and F. Mauri, Density functional perturbation theory for gated two-dimensional heterostructures: Theoretical developments and application to flexural phonons in graphene, Phys. Rev. B **96**, 075448 (2017).

[40] M. Dion, H. Rydberg, E. Schröder, D. C. Langreth, and B. I. Lundqvist, Van der Waals Density Functional for General Geometries, Phys. Rev. Lett. **92**, 246401 (2004).

[41] K. Berland and P. Hyldgaard, Exchange functional that tests the robustness of the plasmon description of the van der Waals density functional, Phys. Rev. B **89**, 035412 (2014).

[42] K. Berland, V. R. Cooper, K. Lee, E. Schröder, T. Thonhauser, P. Hyldgaard, and B. I. Lundqvist, van der Waals forces in density functional theory: A review of the vdW-DF method, Rep. Prog. Phys. **78**, 066501 (2015).

[43] P. Borlido, T. Aull, A. W. Huran, F. Tran, M. A. L. Marques, and S. Botti, Large-Scale Benchmark of Exchange–Correlation Functionals for the Determination of Electronic Band Gaps of Solids, J. Chem. Theory Comput. **15**, 5069 (2019).

[44] N. Marzari, A. A. Mostofi, J. R. Yates, I. Souza, and D. Vanderbilt, Maximally Localized Wannier Functions: Theory and Applications, Rev. Mod. Phys. **84**, 1419 (2012).

[45] G. Pizzi *et al.*, Wannier90 as a community code: New features and applications, J. Phys.: Condens. Matter **32**, 165902 (2020).

[46] Q. Wu, S. Zhang, H.-F. Song, M. Troyer, and A. A. Soluyanov, WannierTools: An open-source software package for novel topological materials, Comput. Phys. Commun. **224**, 405 (2018).

[47] A. A. Soluyanov and D. Vanderbilt, Computing topological invariants without inversion symmetry, Phys. Rev. B **83**, 235401 (2011).

[48] R. Yu, X. L. Qi, A. Bernevig, Z. Fang, and X. Dai, Equivalent expression of $\mathbb{Z}_2$ topological invariant for band insulators using the non-Abelian Berry connection, Phys. Rev. B **84**, 075119 (2011).

[49] C. Sgiarovello, M. Peressi, and R. Resta, Electron localization in the insulating state: Application to crystalline semiconductors, Phys. Rev. B **64**, 115202 (2001).

[50] L. Fu and C. L. Kane, Topological insulators with inversion symmetry, Phys. Rev. B **76**, 045302 (2007).

[51] C.-C. Liu, H. Jiang, and Y. Yao, Low-energy effective Hamiltonian involving spin-orbit coupling in silicene and two-dimensional germanium and tin, Phys. Rev. B **84**, 195430 (2011).

[52] X. Wu, M. Fink, W. Hanke, R. Thomale, and D. Di Sante, Unconventional superconductivity in a doped quantum spin Hall insulator, Phys. Rev. B **100**, 041117(R) (2019).

[53] G. Prandini, A. Marrazzo, I. E. Castelli, N. Mounet, and N. Marzari, Precision and efficiency in solid-state pseudopotential calculations, npj Comput. Mater. **4**, 72 (2018).

[54] N. Marzari, D. Vanderbilt, A. De Vita, and M. C. Payne, Thermal Contraction and Disordering of the Al(110) Surface, Phys. Rev. Lett. **82**, 3296 (1999).

[55] M. J. van Setten, M. Giantomassi, E. Bousquet, M. J. Verstraete, D. R. Hamann, X. Gonze, and G. M. Rignanese, The PseudoDojo: Training and grading a 85 element optimized norm-conserving pseudopotential table, Comput. Phys. Commun. **226**, 39 (2018).

[56] J. P. Perdew, K. Burke, and M. Ernzerhof, Generalized Gradient Approximation Made Simple, Phys. Rev. Lett. **77**, 3865 (1996).

[57] J. Heyd, G. E. Scuseria, and M. Ernzerhof, Hybrid functionals based on a screened Coulomb potential, J. Chem. Phys. **118**, 8207 (2003).

[58] D. R. Hamann, Optimized Norm-Conserving Vanderbilt Pseudopotentials, Phys. Rev. B **88**, 085117 (2013).

[59] M. Schlipf and F. Gygi, Optimization algorithm for the generation of ONCV pseudopotentials, Comput. Phys. Commun. **196**, 36 (2015).

[60] P. Scherpelz, M. Govoni, I. Hamada, and G. Galli, Implementation and validation of fully relativistic GW calculations: Spin–orbit coupling in molecules, nanocrystals, and solids, J. Chem. Theory Comput. **12**, 3523 (2016).

[61] K. Momma and F. Izumi, *VESTA3* for three-dimensional visualization of crystal, volumetric and morphology data, J. Appl. Crystallogr. **44**, 1272 (2011).